# Infrared Signatures of $HNO_3$ and $NO_3^-$ at a Model Aqueous Surface. A Theoretical Study†

**Roberto Bianco,*,‡ Shuzhi Wang,‡ and James T. Hynes*,‡,§**

*Department of Chemistry and Biochemistry, University of Colorado, Boulder, Colorado 80309-0215, and Département de Chimie, CNRS UMR 8640 PASTEUR, Ecole Normale Supérieure, 24 rue Lhomond, Paris 75231, France*

*Received: March 25, 2008; Revised Manuscript Received: June 18, 2008*

The infrared signatures of nitric acid $HNO_3$ and its conjugate anion $NO_3^-$ at the surface of an aqueous layer are derived from electronic structure calculations at the HF/SBK+∗ level of theory on the $HNO_3 \cdot (H_2O)_3 \rightarrow NO_3^- \cdot H_3O^+ \cdot (H_2O)_2$ model reaction system embedded in clusters comprising 33, 40, 45, and 50 classical, polarizable waters, mimicking various degrees of solvation [Bianco, R.; Wang, S.; Hynes, J. T. *J. Phys. Chem. A* **2007**, *111*, 11033]. The molecular level character of the various bands is discussed, and the solvation patterns are described in terms of hydrogen bonding and resulting polarization of the species' intramolecular bonds. Connection is made with assorted experimental results, including surface-sensitive Sum Frequency Generation spectroscopy of aqueous nitric acid solutions, infrared spectroscopy of amorphous thin films of nitric acid monohydrate (NAM) and dihydrate (NAD), and infrared and Raman spectroscopic results for bulk aqueous solutions of nitric acid and nitrate salts.

## 1. Introduction

Vibrational spectroscopy is a powerful tool for the identification and characterization of atmospheric aerosols.[1–12] An aerosol's surface is an especially important region since its microscopic character can determine the chemical reactivity of atmospheric adsorbates. The surface speciation of atmospheric aerosols containing a strong acid such as $HNO_3$ is particularly important due to its possible catalytic effect on heterogeneous chemical reactions. This issue and related questions centered on $HNO_3$ dissociation are relevant in assorted locations in the atmosphere.[13–25]

We have examined via electronic structure calculations the surface dissociation of $HNO_3$[26] and $H_2SO_4$[27,28] in an aqueous environment. At variance with the common perception of both $HNO_3$ and $H_2SO_4$ as "strong" acids, we have found, especially for $HNO_3$, that their acid dissociation at the surface is generally inhibited by lack of sufficient solvation in a wide temperature range of atmospheric relevance.[26–30] Our finding that $HNO_3$ does not acid dissociate at an aqueous surface[26] is consistent with very recent surface spectroscopy experiments[12] concluding that molecular $HNO_3$ is present at the surface, and has also been supported by Car−Parrinello Molecular Dynamics simulations.[31] Our finding is also consistent with an earlier study[32] on the kinetics of dissociation of $HNO_3$ at an ice surface at 150 K, where an experimental activation energy of $0 \pm 2$ kcal/mol was derived. It was argued that the acid would dissociate *after* diffusing by ∼4−7 Å into the surface layer, distances slightly longer than those represented in our models for $HNO_3$ embedding. The presence of residual undissociated $HNO_3$ was detected throughout the kinetic experiments.[32]

In this paper, we examine the (fundamental) vibrational signatures of $HNO_3$ and its acid dissociation product nitrate anion $NO_3^-$ at an aqueous surface for the four model cases reported in ref 26, corresponding to varying degrees of solvation, i.e., hydrogen(H)-bonding. It is found that the frequencies, characters, and intensities of the various vibrations vary, often significantly, with the degree and character of the solvation. For $HNO_3$, these calculated signatures can provide valuable guides for the experimental characterization of both the presence and solvation environment of this predicted molecular species at the aqueous interface. For the $NO_3^-$ anion, there is ample precedent for such qualitative behavior in bulk aqueous solution experimental studies, often involving cationic counterions and ion pairs.[1–3,10,12,33–37] Solvent interactions in an aqueous medium are sufficiently strong to distort the structure of a "free" $NO_3^-$ anion, lift the degeneracy of two of its bands, and render all its six vibrational modes both Raman- and infrared-active.[38]

In the calculations of ref 26 which provide the basis for the present vibrational study, the $HNO_3$ acid dissociation producing $NO_3^-$ in a contact ion pair with a hydronium ion $H_3O^+$ is thermodynamically disfavored at an aqueous surface throughout the 0−300 K temperature range. This conclusion notwithstanding, we have included $NO_3^-$ in the present study as an aide for establishing the predicted absence of this anion via this source in the interfacial region or even establishing its presence, should the free energy calculations of ref 26 prove to be insufficiently accurate or not carried out for a sufficient number of surface configurational cases. The $NO_3^-$ vibrational study should also be useful for experimental investigations of theoretical predictions[39–41] of the affinity of this anion for an aqueous surface region, although the cited studies do not address any acid dissociation issues and thus do not involve the $NO_3^- \cdot H_3O^+$ contact ion pair. Finally, our present focus is exclusively on the infrared signatures for $HNO_3$ and $NO_3^-$. This is a necessary first step toward the much more complex theoretical calculation[42–46] of a surface-sensitive Sum Frequency Generation (SFG) spectrum.[7,8,10,12]

The outline of the remainder of this paper is as follows. The methodology is highlighted in section 2, while the resulting predictions of the vibrational patterns of $HNO_3$ and $NO_3^-$ in surfacial aqueous layers as a function of solvation are presented in section 3. Concluding remarks are offered in section 4.

† Part of the "Stephen R. Leone Festschrift".

* To whom correspondence should be addressed. E-mail: roberto.bianco@colorado.edu (R.B.); hynes@spot.colorado.edu, hynes@chimie.ens.fr (J.T.H.).

‡ University of Colorado.

§ CNRS UMR 8640 PASTEUR, Ecole Normale Supérieure.

10.1021/jp802563g CCC: $40.75 
Published on Web 08/20/2008

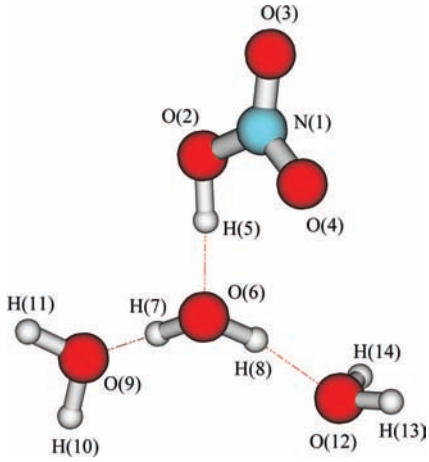


**Figure 1.** Core reaction system (CRS) atomic labeling.

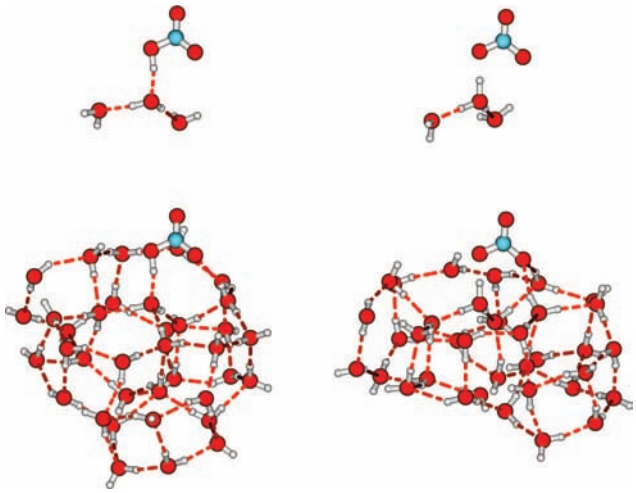

**Figure 2.** Model reaction system (MRS) **I**, $HNO_3 \cdot (H_2O)_3 \cdot W_{33} \rightarrow NO_3^- \cdot H_3O^+ \cdot (H_2O)_2 \cdot W_{33}$. Left: RC. Right: PC. Top row: CRS translated by 10 Å above its image within the MRS. Bottom row: MRS. Structure orientation: the oxygen O(6) of the proton-accepting water in the CRS (see Figure 1) within the MRS is located in the origin of the reference frame; the proton-bearing oxygen O(2) of $HNO_3$ is located on the positive *x* semiaxis, lying within the page and pointing up; the nitrogen N(1) is located in the *xy* plane (page plane). This figure reproduces a portion of Figure 2 of ref 26.

## 2. Methodology

In our previous effort,[26] the acid dissociation of $HNO_3$ adsorbed on the surface of an aqueous layer was modeled in terms of the H-bonded pairs $HNO_3 \cdot H_2O$ and $NO_3^- \cdot H_3O^+$ embedded in large water clusters with various degree of solvation (i.e., H-bonding) for the nitrate group oxygens. In particular, we used the model reaction systems (MRS) $HNO_3 \cdot (H_2O)_3 \cdot W_n \rightarrow NO_3^- \cdot H_3O^+ \cdot (H_2O)_2 \cdot W_n$, with $n = 33$, 40, 45, and 50, where the core reaction system (CRS) $HNO_3 \cdot (H_2O)_3 \rightarrow NO_3^- \cdot H_3O^+ \cdot (H_2O)_2$, cf. Figure 1, was described quantum chemically at the HF/SBK+∗ level of theory,[47–49] and the W's represent classical, polarizable waters,[50] mimicking a water layer. The quantum chemistry program GAMESS[51] was used for the calculations. The reactant complexes (RCs) and product complexes (PCs) for these four cases, labeled **I**−**IV**, are displayed in Figures 2–5. In each case, the RC and PC minima have been derived from a common transition state[26] via a reaction path calculation, followed by full optimization and verification by a vibrational frequency calculation.[26]

Turning to the focus of the present paper, the calculated (fundamental) vibrational frequencies for the CRS intramolecular

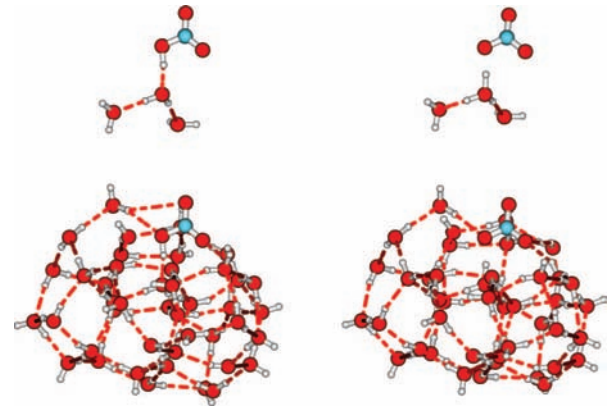

**Figure 3.** MRS **II**, $HNO_3 \cdot (H_2O)_3 \cdot W_{40} \rightarrow NO_3^- \cdot H_3O^+ \cdot (H_2O)_2 \cdot W_{40}$. See Figure 2 for explanation. This figure reproduces a portion of Figure 3 of ref 26.

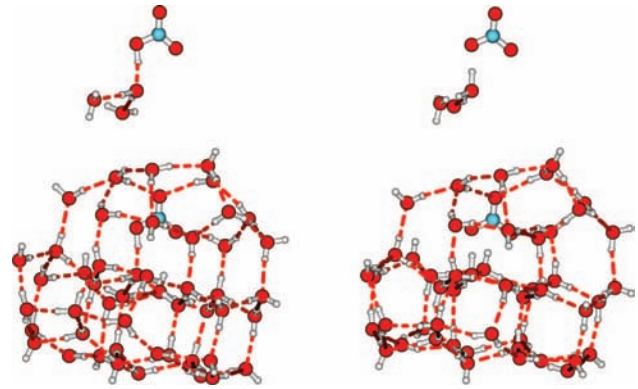

**Figure 4.** MRS **III**, $HNO_3 \cdot (H_2O)_3 \cdot W_{45} \rightarrow NO_3^- \cdot H_3O^+ \cdot (H_2O)_2 \cdot W_{45}$. See Figure 2 for explanation. This figure reproduces a portion of Figure 4 of ref 26.

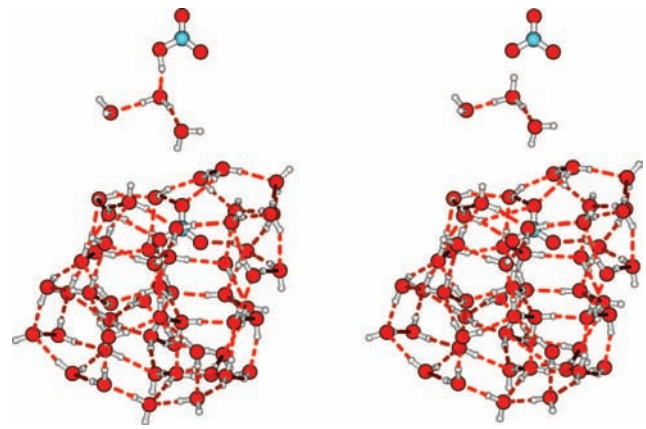

**Figure 5.** MRS **IV**, $HNO_3 \cdot (H_2O)_3 \cdot W_{50} \rightarrow NO_3^- \cdot H_3O^+ \cdot (H_2O)_2 \cdot W_{50}$. See Figure 2 for explanation. This figure reproduces a portion of Figure 5 of ref 26.

modes—the classical waters in the MRS do not contribute intramolecular frequencies since their internal structure is frozen—have been scaled by mode-specific factors derived from the comparisons of the normal modes and frequencies calculated for the isolated, gas phase $HNO_3$, $NO_3^-$, $H_2O$, and $H_3O^+$ species with their experimental equivalents.[26] Application of these mode-specific scaling factors to the frequencies of the solvated species in the water clusters has required the automated identification of the intramolecular, atomic motion components in each mode, verified visually using Molden,[52] and matched to the most similar intramolecular modes of the corresponding gas phase species. The resulting assignments are collected in

**TABLE 1: $HNO_3$ and $NO_3^-$ Mode-Specific Scaled Intramolecular Vibrational Bands for Cases I−IV[a]**

| I | II | III | IV |
|---|---|---|---|
| $\bar{\nu}$/int mode | $\bar{\nu}$/int mode | $\bar{\nu}$/int mode | $\bar{\nu}$/int mode |
| | | $HNO_3$ RC | |
| 618/*0.0* O(2),O(4) bnd | 654/*0.4* O(3) ip rck | 628/*0.1* O(2),O(4) bnd | 643/*0.2* O(2),O(4) bnd |
| 654/*0.6* O(3) ip rck | 778/*0.6* N oop def | 662/*0.5* O(3) ip rck | 661/*0.8* O(3) ip rck |
| 778/*0.4* N oop def | 780/*0.4* N oop def | 786/*0.6* N oop def | 783/*0.5* N oop def |
| 909/*1.4* N−O(2) st | 916/*1.6* N−O(2) st | 923/*0.9* N−O(2) st | 925/*0.9* N−O(2) st |
| 944/*6.5* HONO tors | 996/*4.4* HONO tors | 1085/*3.1* HONO tors | 997/*8.6* HONO tors |
| 1403/*7.7* O(2),O(4) a-st | 1404/*9.1* O(2),O(4) a-st | 1413/*20.5* HON bnd/O(2),O(3) a-st | 1410/*21.8* HON bnd/O(2),O(3) a-st |
| 1457/*15.5* HON bnd | 1456/*17.0* HON bnd/N−O(3) st | 1431/*6.4* HON bnd/O(2),O(4) a-st | 1465/*8.3* HON bnd/N−O(4) st |
| 1704/*11.2* O(3),O(4) a-st[b] | 1687/*9.9* HON bnd/O(3),O(4) a-st | 1689/*7.7* HON bnd/ O(3),O(4) a-st | 1675/*7.4* HON bnd /O(3),O(4) a-st |
| 2930/*43.0* O−H st | 2648/*61.3* O−H st | 2622/*60.9* O−H st | 2557/*66.3* O−H st |
| | | $NO_3^-$ PC | |
| 705/*0.9* O(2),O(4) scs | 727/*0.2* O(4) ip rck | 728/*0.2* O(4) ip rck | 737/*0.1* O(4) ip rck |
| 752/*0.6* O(2),O(3) scs | 763/*0.6* O(2),O(3) scs | 762/*0.8* O(2) ip rck | 790/*0.3* O(2) ip rck |
| 819/*0.7* N oop def | 819/*0.5* N oop def | 825/*0.5* N oop def | 818/*0.4* N oop def |
| 1030/*3.6* O(2),O(4) s-st | 1040/*4.0* O(2),O(4) s-st | 1053/*1.8* O(2),O(4) s-st | 1051/*2.6* O(3),O(4) s-st |
| 1301/*21.9* O(2),O(4) a-st[c] | 1320/*26.7* O(2),O(4) a-st[c] | 1357/ *29.0* N−O(2) st ($H_3O^+$ umb) | 1327/*25.5* N−O(2) st[c] |
| 1508/*24.6* N−O(3) st[c] | 1468/*23.8* N−O(3) st[c] | 1454/*24.3* N−O(3) st | 1466/*17.6* O(3),O(4) a-st[c] |

[a] Mode-specific scaled HF/SBK+* frequencies $\bar{\nu}$ in $cm^{-1}$. IR intensities (int) in $D^2/(amu\ Å^2)$. The notation A(n) identifies atom A with label n in Figure 1. $H_2O(6)$ is the water becoming $H_3O^+$. $H_2O(9)$ and $H_2O(12)$ are the two waters H-bonded to $H_3O^+$. Mode identification: st = stretch, s = symmetric, a = antisymmetric, bnd = bend, def = angular deformation, rck = rocking, scs = scissor, umb = umbrella, ip = in-plane, oop = out-of-plane. For $HNO_3$: *O(i),O(j) bnd* = O(i)−N−O(j) bnd; *O(i),O(j) a/s-st* = O(i)−N−O(j) a/s-st. For $H_2O$: *O(i) bnd* = H−O(i)−H bnd; *O(i) a/s-st* = H−O(i)−H a/s-st. For $H_3O^+$: *def* is an angular deformation involving two Hs; *O−H(i) st* = O(6)−H(i) st; *H(i),H(j) a/s-st* = H(i)−O(6)−H(j) a/s-st. For $NO_3^-$: see $HNO_3$ modes' legend. *Mode A/mode B* = mostly mode A coupled to mode B. *Mode A (mode B)* = predominantly mode A weakly coupled to mode B. [b] Coupled to HON bnd. [c] Weakly coupled to $H_3O^+$ def.

**TABLE 2: $H_2O$ and $H_3O^+$ Mode-Specific Scaled Intramolecular Vibrational Bands for Cases I−IV[a]**

| I | II | III | IV |
|---|---|---|---|
| $\bar{\nu}$/int mode | $\bar{\nu}$/int mode | $\bar{\nu}$/int mode | $\bar{\nu}$/int mode |
| | | $H_2O$ RC | |
| 1653/*3.5* O(12) bnd | 1681/*0.9* O(6)/O(9) bnds | 1675/*3.9* O(12) bnd | 1690/*6.0* O(9) bnd |
| 1688/*4.1* O(9) bnd | 1690/*6.8* O(12) bnd | 1690/*3.8* O(9)/O(6) bnds | 1692/*3.0* O(12) bnd |
| 1711/*2.5* O(6) bnd | 1704/*2.7* O(6)/O(9) bnds | 1706/*5.3* O (6) bnd | 1704/*3.5* O(6) bnd |
| 3418/*16.7* O(6) s-st | 3373/*19.4* O(6) s-st | 3326/*23.7* O(6)−H(7) | 3359/*16.2* O(6) s-st |
| 3462/*21.9* O(6) a-st | 3408/*27.3* O(6) a-st | 3428/*22.8* O(6)−H(8) st | 3372/*30.0* O(6) a-st |
| 3531/*2.8* O(9) s-st | 3485/*4.1* O(9) s-st | 3496/*4.3* O(9) O−H st | 3502/*4.5* O(9) s-st |
| 3589/*2.3* O(9) s-st | 3557/*2.6* O(12) s-st | 3582/*2.8* O(12) s-st | 3552/*3.3* O(12) s-st |
| 3606/*8.9* O(9) a-st | 3604/*8.2* O(9) a-st | 3603/*8.4* O(9) a-st | 3603/*9.2* O(12) a-st |
| 3657/*7.2* O(12) a-st | 3607/*8.9* O(12) a-st | 3643/*8.0* O(12) a-st | 3614/*7.8* O(9) a-st |
| | | $H_2O$ PC | |
| 1647/*3.4* O(12) bnd | 1698/*4.7* O(9) bnd | 1676/*3.2* O(12) bnd | 1701/*4.8* O(12) bnd |
| 1699/*4.3* O(9) bnd | 1710/*3.2* O(12) bnd | 1703/*3.5* O(9) bnd | 1702/*2.0* O(9) bnd |
| 3473/*7.3* O(9)−H(11) st | 3373/*10.6* O(9)−H(11) st | 3374/*10.1* O(9)−H(11) st | 3401/*9.6* O(9)−H(11) st |
| 3552/*3.9* O(12) s-st | 3496/*5.1* O(12) s-st | 3542/*4.2* O(12) s-st | 3472/*6.4* O(12) s-st |
| 3559/*9.3* O(9)−H(10) st | 3540/*10.5* O(12) a-st | 3544/*9.4* O(9)−H(10) st | 3529/ *10.4* O(12)−H(14) st |
| 3619/*8.2* O(12) a-st | 3543/*9.3* O(9)−H(10) st | 3593/*9.4* O(12) a-st | 3566/*8.2* O(9)−H(10) st |
| | | $H_3O^+$ PC | |
| 1385/*3.0* umb | 1405/*4.6* umb | 1446/*1.5* umb | 1380/*8.6* umb |
| 1804/*0.6* def | 1751/*2.0* def (O(12) bnd) | 1773/*0.7* def (O(12) bnd) | 1745/*5.6* def |
| 1806/*0.7* H(8) rck | 1819/*0.0* def | 1830/ *0.3* def | 1834/*1.0* def |
| 2272/*81.7* O−H(5) st | 2129/*89.0* O−H(5) st | 2368/*96.9* O−H(5) st | 2253/*90.5* O−H(5) st |
| 2990/*53.5* O−H(7) st | 2803/*60.0* O−H(7) st | 2626/*53.8* O−H(7) st | 2785/*66.7* H(7),H(8) a-st |
| 3128/*26.6* O−H(8) st | 3001/*30.8* O−H(8) st | 3030/*34.3* O−H(8) st | 2918/*24.2* H(7),H(8) s-st |

[a] See Table 1 for legend.

Tables 1 ($HNO_3$ and $NO_3^-$) and 2 ($H_2O$ and $H_3O^+$), containing the mode-specific scaled intramolecular vibrational frequencies for cases **I**−**IV**; the reader is referred to those tables for the ensuing discussion. We refer to either a band or a spectral region by its wavenumber/s only, while omitting the units.

In GAMESS,[51] vibrational intensities are calculated as the square of the projection of the dipole derivative tensor onto each normal mode. For closed shell molecules of size similar to the species considered here, the HF method with split-valence basis sets complemented by polarized and diffused functions, similar to the SBK+* used here, can predict with qualitative accuracy both the ordering and relative ratios of the infrared intensities.[53] In this work, the intensities have not been scaled.

### 3. Infrared Signatures of $HNO_3$ and $NO_3^-$ at an Aqueous Layer

**3.1. Overview.** We display the vibrational modes of gas phase $HNO_3$ and $NO_3^-$ in Figures 6 and 7, respectively, to assist in our discussion of the vibrational signatures at an aqueous surface. The vibrational spectra in Figure 8 include the calculated

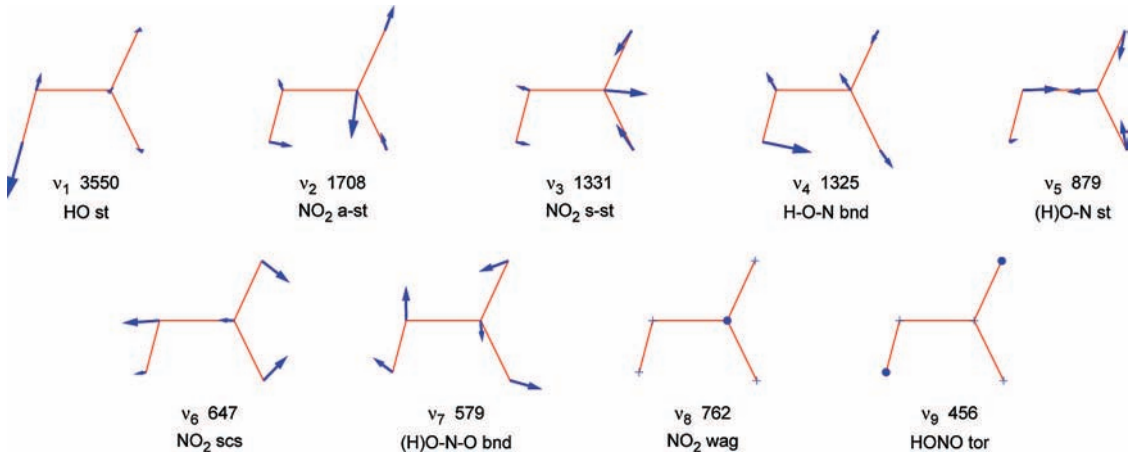


**Figure 6.** Vibrational mode characterization of gas phase, isolated $HNO_3$. Frequencies in $cm^{-1}$. See Table 1 for legend. Large dots and plus signs on the atomic centers represent vectors pointing up and down, respectively, from the plane of the page.

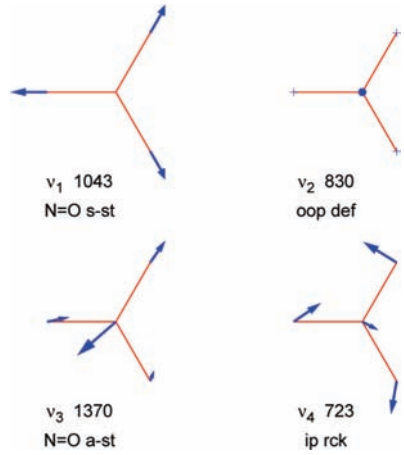


**Figure 7.** Vibrational mode characterization of gas phase, isolated $NO_3^-$. Frequencies in $cm^{-1}$. The bands $\nu_3$ 1370, N═O a-st, and $\nu_4$ 723, in-plane bnd, are doubly degenerate. See Table 1 for legend and Figure 6 for explanation.

intramolecular bands of the $HNO_3$, $H_2O$, $NO_3^-$ and $H_3O^+$ species in the RC and PC of cases **I**−**IV**. The intramolecular modes were selected among the several hundreds calculated for each RC/PC by (i) summing the norms of the atomic components of motion for each mode of each of the $HNO_3$, $NO_3^-$, $H_2O$ and $H_3O^+$ species, and (ii) retaining the first $n$ modes with the largest sum, with $n$ the number of vibrational modes for each species as if considered in isolation (e.g., nine modes for $HNO_3$). The final characterizations were verified visually via animation of the selected modes using Molden[52] (the remaining, numerous calculated modes/frequencies unfit for the selection criterion are available as Supporting Information).

The overview displayed in the top panel of Figure 8 comprises the calculated bands for MRS **I**−**IV** RCs and PCs, whereas the middle and bottom panels contain, respectively, the $HNO_3$ and $H_2O$ bands for the RCs, and the $NO_3^-$, $H_3O^+$, and $H_2O$ bands for the PCs. The vibrational patterns are grouped into five spectral regions: (1) 600−1100: $NO_3$ group bends and low-frequency stretches, together with the HONO torsion in $HNO_3$; (2) 1300−1500: other $NO_3$ group stretches, from both $HNO_3$ and $NO_3^-$, and the $H_3O^+$ umbrella mode; (3) 1600−1900: a $HNO_3$ band, corresponding to a coupled HON bend/$NO_2$ antisymmetric stretch, and the $H_2O$ and $H_3O^+$ bends; (4) 2100−3200: H−$ONO_2$ and $H_3O^+$ stretches; (5) 3300−3700: $H_2O$ stretches. In the ensuing discussion, consistent with our stated focus, we focus primarily on the $HNO_3$ and $NO_3^-$ bands and their associated experimental features[2,3,12,35] in sections 3.2, 3.3, and 3.4. We display all $H_2O$ and $H_3O^+$ bands for the regions examined as a background for the $HNO_3/NO_3^-$ features without, however, discussing them.

In order to avoid incessant repetition throughout the subsequent discussion, the reader is assumed to refer to Figure 1 for the atomic labeling, to Table 1 for the assignments of the $HNO_3$ and $NO_3^-$ bands in Figures 8–12 (the $H_2O$ and $H_3O^+$ bands are reported in Table 1 for reference, without however an accompanying discussion, given the absence of "dangling" OH bonds in our model reaction systems, and the large variability of OH stretches' frequencies in condensed phase, their validity for assignment purposes is limited), to Table 3 for a collection of experimental vibrational bands assigned to $HNO_3$ and $NO_3^-$ in various aqueous environments,[2,3,12,35] to Table 4 for the H-bonding patterns of $HNO_3$ and $NO_3^-$, to Table 5 for some key bond lengths in the CRS, and to Table 6 for the atomic charges of $HNO_3$ and $NO_3^-$. To facilitate appreciation of frequency shifts with the degree of solvation, we denote a mode by all its mode-specific scaled frequencies in the four cases examined, ordered from the lowest to the highest solvation, i.e., $\bar{\nu}_{\mathbf{I}}/\bar{\nu}_{\mathbf{II}}/\bar{\nu}_{\mathbf{III}}/\bar{\nu}_{\mathbf{IV}}$. In case **III**, $HNO_3$ in the RC lacks a H-bond on the proton-bearing O(2), resulting in a stronger N═O(2) double bond character; its effects will appear throughout the discussion.

Before proceeding, we remark that an analysis of the O−H and H-bond distances in the CRS PC for **I**−**IV** (cf. Table 7) shows that the contact ion pair (CIP) formed in the acid dissociation involves an Eigen-like hydronium cation $H_3O^+$ rather than a Zundel cation $H_5O_2^+$ (with the proton shared between two waters), as noted in ref 26 (see also ref 54). This picture was confirmed via vibrational analysis, with the six bands characterizing $H_3O^+$ all clearly identifiable (see Table 2), and none of them involving bands in the vicinity of the broad proton oscillation band at 1055 $cm^{-1}$ typical of a partially solvated Zundel cation.[55] (We note in this connection the previous theoretical findings of $H_3O^+$ in CIPs for the acid dissociations of HCl[56,57] and HF[58] in aqueous solution, and of HCl,[59,60] HBr,[34] and $H_2SO_4$[27,28] at model aqueous surfaces; for a recent experimental example, see ref 61).

We now discuss in turn the calculated spectral features of $HNO_3$ and $NO_3^-$ in the various frequency regions, together with assorted experimental results where available. Only the peaks of the experimental bands, taken from Table 2, are shown, with arbitrary intensities, and we also use the band terminology for the theoretical frequency values.

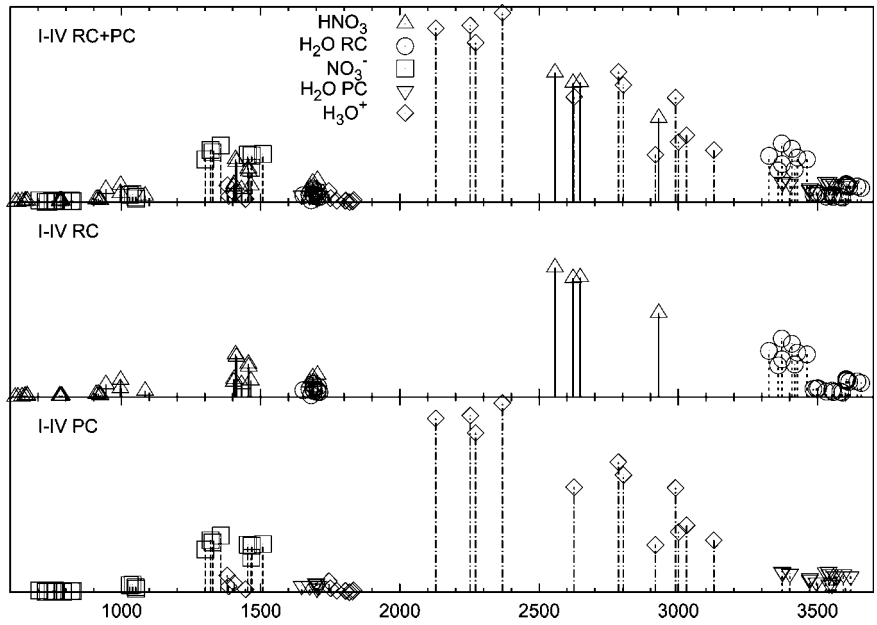


**Figure 8.** Calculated $HNO_3$, $H_2O$, $NO_3^-$, and $H_3O^+$ infrared bands in the 600−3700 $cm^{-1}$ interval for MRS cases **I**−**IV**. Triangles: $HNO_3$ in RC. Circles: $H_2O$ in RC. Squares: $NO_3^-$ in PC. Inverted triangles: $H_2O$ in PC. Diamonds: $H_3O^+$ in PC. Filled triangles: $HNO_3$ experimental bands from ref 12 (arbitrary intensities). The ordinate axis spans the [0,100] $D^2$/(amu Å$^2$) interval.

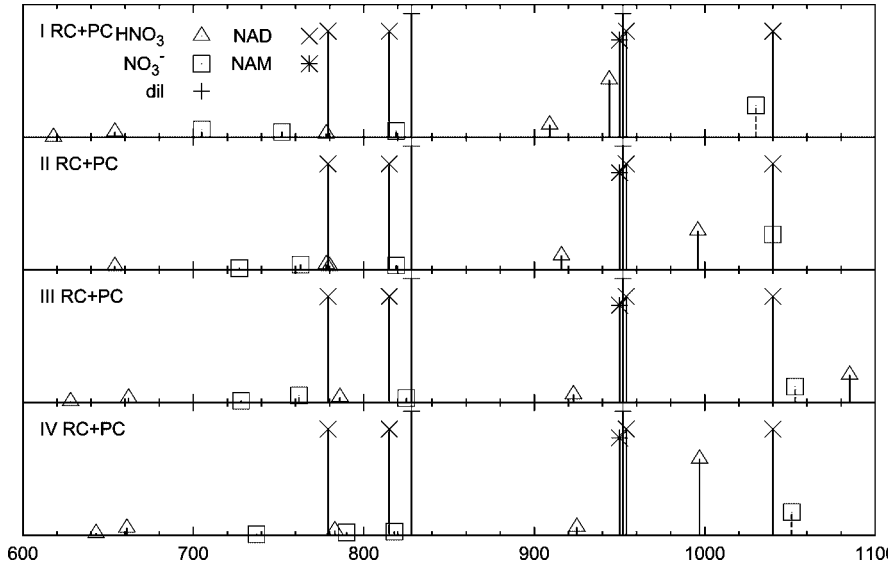


**Figure 9.** $HNO_3$ and $NO_3^-$ infrared bands in the 600−1100 $cm^{-1}$ interval for MRS **I**−**IV**. The ordinate axis spans the [0,15] $D^2$/(amu Å$^2$) interval. See Figure 8 and Table 3 for legend.

**3.2. The 600−1100 $cm^{-1}$ Region (Figure 9).** ***3.2.1. $HNO_3$.*** $HNO_3$ has two angular in-plane deformations: the O(2)−N−O(4) bending at 618/-/628/643 (this mode was not found for **II**) and the O(3) in-plane rocking at 654/654/662/661. Another $HNO_3$ band at 778/(778,780)/786/783 corresponds to the $NO_3$ out-of-plane deformation—note that this band is quasi-degenerate in **II**, similar to the isolated species, suggesting an environment where the distortions parallel to the $NO_3$ plane are presumably minor. The out-of-plane deformation of the $NO_3$ group shows a mild blue-shift with increased solvation, suggesting that the higher degree of H-bonding to the $NO_3$ oxygens constitutes but a small perturbation by the H-bonding environment. This band corresponds to the 779 band in NAD (nitric acid dihydrate).

The N−O(2) stretch in $HNO_3$ at 909/916/923/925 has a solvation pattern consistent with a mild increase in H-bonding to O(3) and O(4), which results in an electronic polarization of the $NO_3$ group enhancing the double bond character of N−O(2) and, in turn, also increasing the acidity of the O(2)-bound proton (the acidity of $HNO_3$ in **I**−**IV** has been extensively discussed in ref 26). Although this band appears to be the closest to the cluster of experimental bands at 950−960, it is evidently not a match due to its low intensity which, presumably, prevents its identification in experimental spectra.

The last $HNO_3$ band in this region appears at 944/996/1085/997 and corresponds to the HONO torsion. The marked variability of this band is due to its sensitivity to the solvation environment: with the proton strongly H-bonded to the acceptor water, the frequency of the band increases with the force constant for the rotation of the HO(2) and O(3)−N−O(4) moieties around the N−O(2) axis. In turn, this depends on (i) the degree of H-bonding by the water network to O(3) and O(4), increasing from **I** to **IV**, which leads to a larger double bond character of the N−O(2) bond, and (ii) by direct H-bonding to O(2), which favors, in opposition to the previous effect, the

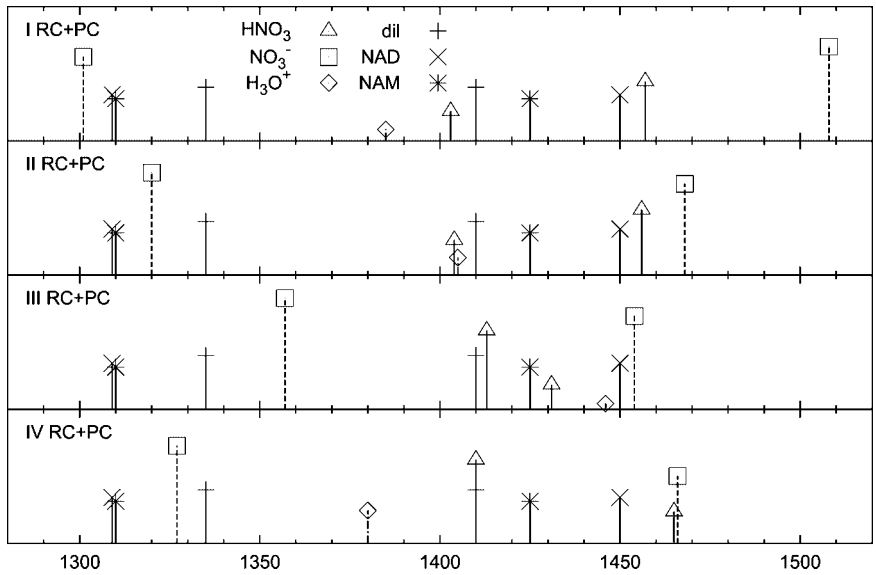


**Figure 10.** $HNO_3$, $NO_3^-$, and $H_3O^+$ infrared bands in the 1280−1520 $cm^{-1}$ interval for MRS **I**−**IV**. The ordinate axis spans the [0,35] $D^2/(amu\ Å^2)$ interval. See Figure 8 and Table 3 for legend.

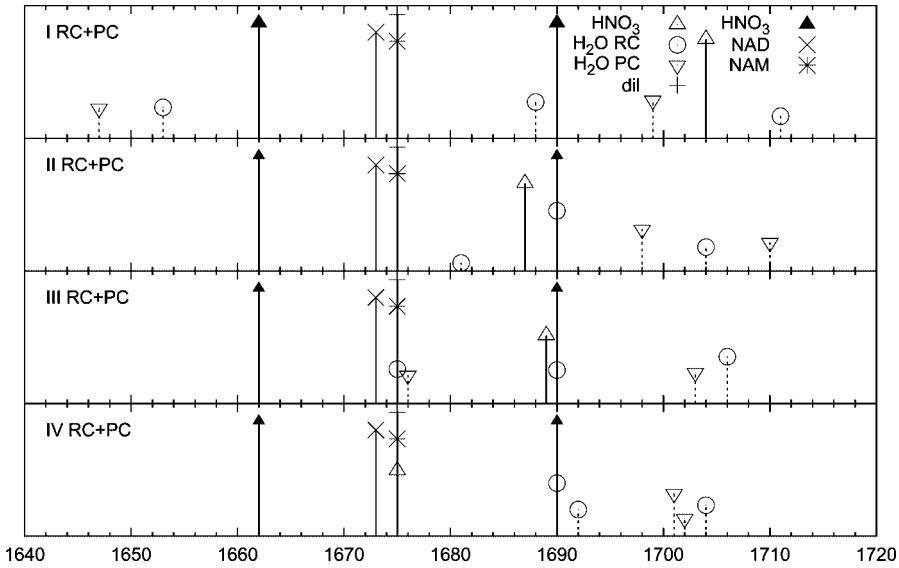


**Figure 11.** $HNO_3$ and $H_2O$ infrared bands in the 1640−1720 $cm^{-1}$ interval for MRS **I**−**IV**. The ordinate axis spans the [0,15] $D^2/(amu\ Å^2)$ interval. See Figure 8 and Table 3 for legend.

localization of the electron density over the O(2) center, and thus a less pronounced N═O(2) double bond character. Consistent with this picture, the absence of H-bonding to O(2) for **III** results in the 1085 band, about 90 $cm^{-1}$ higher than in the other three cases, due to the enhanced N═O(2) bond character. With the exception of **III**, this band is sufficiently close to the 950−960 cluster of experimental bands, assigned to the HONO torsion[35] (see also Table 3).

***3.2.2. $NO_3^-$.*** In general, except for the $HNO_3$ torsion, the $NO_3^-$ bands in this region display a pattern similar to the $HNO_3$ bands, albeit they are all blue-shifted with respect to those, due to the greater N═O bonds' strengths in the $NO_3^-$ anion. The first band at 705/727/728/737 involves in **I** the O(2)−N−O(4) scissoring, but transforms into the O(4) in-plane rocking for the more solvated cases, due to the larger number of H-bonds to O(2) and O(4), which also explains the progressive frequency increase.

The second band at 752/763/762/790 corresponds to the O(2)−N−O(3) scissoring in **I/II**, which is replaced by the in-plane rocking of O(2) in **III/IV**, where H-bonding to O(3) is stronger. This mode, due to the H-bond of O(2) to the hydronium ion, is associated with $NO_3^-/H_3O^+$ contact ion

**TABLE 3: Selected $HNO_3$ and $NO_3^-$ Experimental Vibrational Bands in Various Aqueous Environments**

| mode[a] | NAM[b] | NAD[c] | dil[d] | surface[e] |
|---|---|---|---|---|
| | | $HNO_3$ | | |
| N oop def | | 779 | | |
| HONO tors | 950 | 954 | 952 | |
| HON bnd | 1425 | 1450 | 1410 | |
| HON bnd[f] | 1675 | 1673 | 1675 | 1662/1690 |
| | | $NO_3^-$ | | |
| N oop def | | 815 | 828 | |
| $NO_2$ s-st | | 1040 | | |
| $NO_2$ a-st | 1310 | 1309 | 1335 | |

[a] Our assignments. See Table 1 for legend. [b] Nitric Acid Monohydrate (NAM); Amorphous $HNO_3/H_2O$ 1:1 film. ref 2, Figure 3a therein. [c] Nitric Acid Dihydrate (NAD); Amorphous $HNO_3/H_2O$ 1:2 film. ref 3. [d] Aqueous solution $HNO_3$ 25 wt% ($H_2O/HNO_3$ mole ratio of 10.5). ref 35, Table 4 therein. [e] Surface vibrational spectroscopy, ref 12. [f] Coupled to the $NO_2$ a-st.

**TABLE 4: H-Bonding Patterns in RC/PC**

| | RC | | PC | |
|---|---|---|---|---|
| **I** | 6 (1.64/169)[a] | | 2 (1.44/179) | PT[b] |
| | 6 (1.92/164) | | 4 (2.08/160) | nhb |
| | | | 2 (2.28/138) | nhb |
| | 4 (2.16/165) | → | 4 (2.01/161) | −0.15 |
| **II** | 6 (1.55/173) | | 2 (1.42/176) | PT |
| | 2 (2.29/156) | → | 2 (2.05/167) | −0.23 |
| | 4 (2.39/147) | → | 4 (2.26/148) | −0.13 |
| | 4 (2.33/142) | → | 4 (2.19/146) | −0.14 |
| **III** | 6 (1.55/172) | | 2 (1.46/177) | PT |
| | | | 4 (2.16/156) | nhb |
| | 3 (2.21/163) | → | 3 (2.18/161) | −0.03 |
| | 4 (2.23/146) | → | 4 (2.07/160) | −0.16 |
| | 3 (2.25/162) | → | 3 (2.14/172) | −0.11 |
| **IV** | 6 (1.52/167) | | 2 (1.43/168) | PT |
| | 4 (2.17/153) | → | 4 (2.07/154) | −0.11 |
| | 3 (2.26/154) | → | 3 (2.15/162) | −0.11 |
| | 3 (2.27/153) | → | 3 (2.17/157) | −0.10 |
| | 2 (2.10/161) | → | 2 (1.96/163) | −0.13 |

[a] In n (h/α): n is the numeric label of the H-bonded O in the CRS labeling scheme in Figure 1, h is the H···O(n) distance in Å, α is the O−H···O(n) angle in deg. [b] PT: H-bond deriving from proton transfer (PT). nhb: new H-bond. The numbers in this column represent the H-bond shortening (in Å) in going from RC to PC.

**TABLE 5: Key Bond Lengths in the CRS[a]**

| | **I** | **II** | **III** | **IV** |
|---|---|---|---|---|
| | $HNO_3/NO_3^-$ | $HNO_3/NO_3^-$ | $HNO_3/NO_3^-$ | $HNO_3/NO_3^-$ |
| N(1)−O(2) | 1.32/1.27 | 1.32/1.27 | 1.31/1.26 | 1.31/1.27 |
| N(1)−O(3) | 1.19/1.20 | 1.19/1.21 | 1.20/1.22 | 1.20/1.22 |
| N(1)−O(4) | 1.21/1.25 | 1.21/1.23 | 1.21/1.24 | 1.20/1.22 |
| H(5)−O(2) | 1.00/1.44 | 1.01/1.42 | 1.01/1.46 | 1.02/1.43 |
| H(5)−O(6) | 1.64/1.04 | 1.55/1.05 | 1.55/1.03 | 1.52/1.05 |

[a] Atomic labels as in Figure 1. HF/SBK+* bond lengths in Å. The structures of $HNO_3$ (in RC) and $NO_3^-$ (in PC) are those displayed in Figures 2–5.

**TABLE 6: Charge Distributions of $HNO_3$ and $NO_3^-$[a]**

| | **I** | | **II** | | **III** | | **IV** | |
|---|---|---|---|---|---|---|---|---|
| | $HNO_3$ | $NO_3^-$ | $HNO_3$ | $NO_3^-$ | $HNO_3$ | $NO_3^-$ | $HNO_3$ | $NO_3^-$ |
| N(1) | 0.41 | 0.38 | 0.40 | 0.39 | 0.40 | 0.38 | 0.41 | 0.40 |
| O(2) | −0.39 | −0.50 | −0.40 | −0.51 | −0.37 | −0.46 | −0.41 | −0.51 |
| O(3) | −0.24 | −0.27 | −0.25 | −0.32 | −0.30 | −0.36 | −0.32 | −0.39 |
| O(4) | −0.35 | −0.49 | −0.35 | −0.43 | −0.33 | −0.46 | −0.29 | −0.38 |
| H(5) | 0.49 | 0.51 | 0.50 | 0.51 | 0.50 | 0.51 | 0.50 | 0.51 |

[a] Atomic labels as in Figure 1. HF/SBK+* Löwdin atomic charges in atomic units. The structures of $HNO_3$ (in RC) and $NO_3^-$ (in PC) are those displayed in Figures 2–5.

pairing, and is close to ion pair bands for concentrated aqueous solutions of dissolved nitrate salts and found experimentally at 740[38] (not shown in Figure 9).

The 819/819/825/818 band corresponds to the N vibration out of the $NO_3$ plane, anchored by H-bonding to both the $H_3O^+$ and surrounding waters; as discussed for $HNO_3$, the solvation-induced shift for this band is minimal. The 828 dil and 815 NAD bands show a strong correspondence with this band. (see also Table 3).

The 1030/1040/1053/1051 band corresponds to the O(2)−N−O(4) symmetric stretch for cases **I/II/III**, morphing into the O(3)−N−O(4) symmetric stretch for case **IV**, and is indicative of ion pairing.[38] The mild blue-shift is due to the stabilization of the $NO_3^-$ ion due to increased solvation, thus enhancing its N═O double bond character. Its proximity to all the experimental bands in the 1020−1060 range suggests the presence of contact ion pairs in those environments.

**3.3. The 1280−1520 cm$^{-1}$ Region (Figure 10).** ***3.3.1. $HNO_3$.*** The two $HNO_3$ bands in this region correspond to combinations of the HON bend and/or a $NO_2$ group stretch. In particular, 1403/1404/1431/1465 starts as a O(2)−N−O(4) antisymmetric stretch in **I** and **II**, but acquires a predominant HON bend character in **III** and **IV**, with less important O(2)−N−O(4) antisymmetric stretch and N−O(4) stretch components, respectively. The solvation trend of this band is consistent with a general increase of H-bonding to the O(3)−N−O(4) group, resulting into an increase of the force constant of the HON bend, explained as follows: H-bonding to the $HNO_3$ oxygens determines the character of the N−O(2) bond, i.e., N═O(2) vs $^+$N−O(2)$^-$, with a resulting force constant for the $N^+-O^--H$ bend smaller than that for the N═O−H bend. In addition, since the increase of N═O(2) double bond character involves polarization of the O(2)−H bond, with a concomitant increase in acidity (see Tables 5 and 6, and, more generally, ref 26), the N═O(2)−H···O(6) H-bond strengthens, thus increasing the HON bend force constant—the progressive acquisition of HON bend character with increased solvation results in the blue shift. This band matches best the 1410 dil band, but is also quite close to the 1425 NAM (nitric acid monohydrate) band (see also Table 3).

Conversely, the 1457/1456/1413/1410 band starts as HON bend, but it acquires first N−O(3) stretch character and subsequently O(2)−N−O(3) antisymmetric stretch character. The solvation trend of this band is reversed relative to 1403/1404/1431/1465, previously discussed. Its corresponding experimental band is 1450 NAD in Table 3.

***3.3.2. $NO_3^-$.*** For $NO_3^-$, the very intense 1301/1320/1357/1327 band corresponds to the O(2)−N−O(4) antisymmetric stretch, weakly coupled to a $H_3O^+$ angular deformation for cases **I** and **II**, and to the N−O(2) stretch for cases **III** and **IV**. The blue shift from **I** to **IV** can be explained in terms of the H-bonding to the nitrate oxygens and, since the N−O(2) stretch is a key component in all cases, we focus on the effects of solvation on this bond. Assuming N−O(2) can be described in terms of the two resonance structures $^+$N−O(2)$^-$ and N═O(2), the $^+H_2OH\cdots O(2)-N$ H-bond, as well as any other extra H-bond on O(2), tends to polarize the bond in favor of $^+$N−O(2)$^-$ single bond character. In **I**, there are two H-bonds on O(2) and two on O(4). In **II**, the number and type of H-bonds do not change (albeit from the H-bond lengths one could argue that there should be a red shift of the band), however we note a small 19 cm$^{-1}$ blue shift, which we would ascribe to a more extended solvation environment than that represented in Table 4. In **III**, one H-bond on O(2) is replaced by two H-bonds on O(3), thus adding more N═O(2) character, with a resulting increase in force constant and the largest blue shift relative to **I**. In **IV**, a H-bond on O(4) is replaced by a strong H-bond on O(2), thus decreasing, relative to **III**, the N═O(2) character and the frequency. Also, $\bar{\nu}_{\mathbf{IV}}$ 1327 is blue-shifted relative to $\bar{\nu}_{\mathbf{II}}$ 1320 because of the replacement of a H-bond on O(4) with two stronger H-bonds on O(3). This widely variable band corresponds to the band group comprising 1310 NAM, 1309 NAD, and 1335 dil.

The other intense 1508/1468/1454/1466 band corresponds to the N−O(3) stretch for all cases except **IV**, where it changes to the O(3)−N−O(4) antisymmetric stretch. Since the N−O(3) stretch is always present, we focus on this mode. The N−O(3) bond length increases, accompanied by the increase (in modulo) of the N(1) and O(3) atomic charges, both indicating a decrease

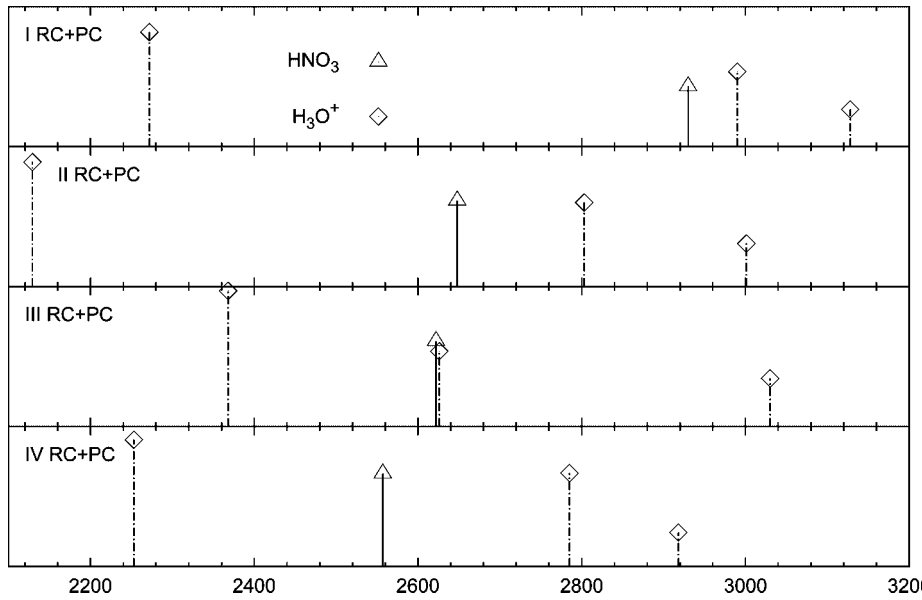


**Figure 12.** $HNO_3$ and $H_3O^+$ infrared bands in the 2100−3200 $cm^{-1}$ interval for MRS **I**−**IV**. The ordinate axis spans the [0,100] $D^2/(amu\ Å^2)$ interval. See Figure 8 for legend.

**TABLE 7: Hydrogen-Bonding Features of the CRS in Figure 1**[a]

| | O(2)−H(5) | H(5)−O(6) | O(6)−H(7) | H(7)−O(9) | O(6)−H(8) | H(8)−O(12) |
|---|---|---|---|---|---|---|
| **I** | 0.997/1.440 | 1.637/1.043 | 0.974/1.001 | 1.781/1.584 | 0.972/0.996 | 1.834/1.631 |
| **II** | 1.014/1.416 | 1.549/1.053 | 0.977/1.012 | 1.757/1.538 | 0.975/1.004 | 1.794/1.592 |
| **III** | 1.014/1.457 | 1.547/1.035 | 0.979/1.024 | 1.736/1.491 | 0.974/1.000 | 1.787/1.590 |
| **IV** | 1.019/1.428 | 1.517/1.045 | 0.977/1.010 | 1.767/1.557 | 0.977/1.011 | 1.751/1.542 |

[a] H(5) is the transferring proton, O(6)H(7)H(8) is the acceptor water, and H(5)O(6)H(7)H(8)$^+$ is the hydronium ion. Distances in Å. The two numbers in each column refer to RC/PC. The HF/SBK+* OH bond length in isolated $H_3O^+$ is 0.9793 Å.

in N═O(3) double bond and an increase in $^+$N−O(3)$^-$ single bond characters, and thus explaining the reported frequency decrease. If we exclude the 1508 band, since it is unlikely that $HNO_3$ can ionize in the conditions mimicked by **I**, this band is well matched to 1450 NAD, leading to the conclusion that the infrared signal in the 1440−1480 region is a superposition of $HNO_3$ and $NO_3^-$ bands.

**3.4. The 1640−1720 $cm^{-1}$ Region (Figure 11).** The single calculated $HNO_3$ 1704/1687/1689/1675 band appears in **I** as the O(3)−N−O(4) antisymmetric stretch, with the HON bend as a lesser component, however the relative contributions of these two modes reverse in **II/III/IV**. The solvation trend of this band is due to a variety of effects. The H-bonding pattern on O(3) and O(4) influences the O(3)−N−O(4) antisymmetric stretch: in **I**, there is only one H-bond in O(4); in **II**, there are two H-bonds on O(4); in **III**, there are two H-bonds on O(3) and one on O(4), in **IV**, there are one H-bond on O(2), two H-bonds on O(3) and one on O(4). The N−O(3) and N−O(4) bond lengths are affected by increasing solvation in opposite ways: the former is lengthening, whereas the latter is shortening. Correspondingly, the O(3) and O(4) atomic charges are becoming, respectively, more and less negative. An increase in electron density on a nitrate oxygen signals a preference for the single bonded $^+$N−O$^-$ vs the double bonded N═O resonance structure. Thus, a contribution to the frequency pattern of this band results from the balance between two opposing polarization trends for the N−O(3) and N−O(4) bonds, whose total effect on the $NO_2$ group antisymmetric stretch should be presumably small. Concerning the HON bend component of this band, both the progressive lengthening of the H−O(2) bond and the increase in N═O(2) double bond vs $^+$N−O(2)$^-$ single bond character, accompanied by the charge distribution increase on H(5) and the concomitant strengthening of the H(5)···O(6) H-bond, contribute to a decrease of the HON bend component frequency. The cumulative effect, with the HON bend predominant in **II/III/IV**, leads to a marked frequency decrease with increased solvation for this band. The calculated frequencies for **II/III/IV** show good agreement with the experimental bands in Table 2, with case **IV**, the most solvated, essentially coinciding with the thin film (NAM and NAD) and bulk ("dil") cases, thus signaling the presence of molecular $HNO_3$ in these samples.

Of particular interest in Figure 11 and Table 3 are the two bands at 1662 and 1690, assigned in ref 12, via a surface-sensitive technique, to the $NO_2$ antisymmetric stretch of molecular $HNO_3$ *at the surface* of several aqueous samples whose bulk solution values of the $NO_3^-/HNO_3$ ratios were estimated to be 3:1, 3:2, and 1:4, with the majority of the surface spectroscopic measurements focused on the latter two cases.[12] In particular, the 1690 band was interpreted as due to a monohydrate complex "on top" of the surface layer, whereas the 1662 band was assigned to a more strongly H-bonded $HNO_3 \cdot (H_2O)_n$ moiety. The agreement of the calculated frequencies 1704 for **I** and 1675 for **IV**, respectively, mimicking the solvation environments hypothesized for the 1690 and 1662 experimental bands, is quite good, thus confirming, in general, the assignments in ref 12, with the added emphasis on the HON bend contribution to the mode, which would suggest significant effects deriving from deuteration. The frequency gap between the experimental bands is 28 $cm^{-1}$, also in good agreement with the calculated one of 29 $cm^{-1}$. Earlier (and more detailed) considerations relating to the identification of these bands have been made in ref 26; here we discuss further aspects. The concentration of molecular $HNO_3$ at the surface is a key difference between the experiments and the calculations. While

the latter represent infinitely diluted situations, in the experiments, $HNO_3-HNO_3$ interactions could also be involved: a $HNO_3$ acidic proton H-bonded to the nitro group of another molecular $HNO_3$ would presumably red-shift this band more than a H-bonded water proton would, by shifting electron density from the N═O bonds onto the oxygens.

**3.5. The 2100−3200 cm$^{-1}$ Region (Figure 12).** In this region, the 2930/2648/2622/2557 OH stretch of $HNO_3$ appears together with the OH stretches of $H_3O^+$. With the exception of 2930 in **I**, 2648/2622/2557 fall in a narrow range at the low frequency edge of the $H_3O^+$ antisymmetric stretch region, well distinguished from the $H_3O^+$ symmetric stretches (see Figure 8). In experimental spectra, the broadband comprising the $H_3O^+$ stretches (which is relatively shallow relative to the strong nitrate group features) envelops the $HNO_3$ OH stretch and decreases its usefulness for identification and interpretation purposes (cf. e.g. Figure 3 in ref 2). In Figure 12, this band red-shifts with increasing solvation due to the weakening of the $H-ONO_2$ bond via H-bonding to the nitrate oxygens in the contact ion pair. The largest red-shift, 282 cm$^{-1}$ from **I** to **II**, corresponds to an increase in H-bonds by the surface waters from a single one, to O(4), to three, two H-bonds to O(4) and one to O(2). This large solvation effect is reflected by the 0.01 au increase of the H(5) atomic charge and the reduction by ∼0.1 Å of the H(5)···O(6) H-bond. From **II** to **III**, the number of H-bonds remains constant, although, for **II**, two H-bonds on O(2) and O(4) are replaced in **III** by two stronger H-bonds on O(3), resulting in a relatively smaller 26 cm$^{-1}$ red-shift. From **III** to **IV**, the additional H-bond on O(2) yields a further red-shift of 65 cm$^{-1}$. The solvation trend for the H−O(2) stretch is consistent with that of the N−O(2) stretch, whose frequency blue-shifts with increased solvation of the $NO_3$ group enhancing the N═O(2) double bond character (see section 3.2.1).

## 4. Concluding Remarks

In this paper, we have examined the (fundamental) vibrational signatures of $HNO_3$ and its acid dissociation product nitrate anion $NO_3^-$ at a model aqueous surface for the four model cases that we have previously reported in ref 26, which reflect varying degrees of solvation. It is found that the frequencies, characters and intensities of the various vibrations vary, often significantly, with the degree and character of the solvation.

For the ion pair product, all the solvation trends in the band patterns can be explained in terms of H-bonding to the $H_2O\cdots HNO_3/H_2OH^+\cdots ONO_2^-$ moieties in the core reaction system (CRS) and the resulting polarization of its $\pi$ electron system, which varies the double bond character of the N−O bonds. For $NO_3^-$, H-bonding affects mostly the modes involving N−O stretches. For $HNO_3$, in addition to the N−O stretches, the HONO torsion is affected via H-bonding to O(2) and the resulting N═O(2) double bond character.

The calculated bands have been connected with surface (as well as bulk) spectroscopic experiments, and it is hoped that the present results will prove useful in the interpretation of these and future experiments designed to probe the atmospherically and environmentally important nitric acid and nitrate ion at aqueous surfaces. As already noted at the end of section 2, our calculated spectral patterns, indicative of the effects of the local environment, should be intended as guidance in the identification of the expected qualitative characteristic features of experimental spectral patterns, rather than quantitative in terms of comparison. The accuracy of the calculated bands, as evinced from the comparisons to experimental bands in the various figures, is roughly within the 10−20 cm$^{-1}$ range. Concerning lineshapes, the effective concentration of the model systems we examined is far more diluted than experimental $HNO_3$ mono-, di-, and trihydrate samples, and does not allow a direct comparison with these systems. Finally, as noted in the Introduction, the present results should also prove of value in future theoretical treatments of surface-sensitive Sum Frequency Generation spectra.[42–46]

**Acknowledgment.** This work was supported in part by NSF grant CHE-0417570. JTH also acknowledges support via an ANR grant (NT05-4-43154) and ECOS grant A01U03. J.T.H. expresses his appreciation for Steve Leone as a colleague and a friend.

**Supporting Information Available:** GAMESS output files for the fully optimized reactant and product complexes of cases **I**−**IV** to be used with Molden[52] for structural analysis and normal mode visualization. Tables with mode number assignments for the GAMESS output files. Instructions for the use of the various files. This material is available free of charge via the Internet at http://pubs.acs.org.

## References and Notes

(1) Ritzhaupt, G.; Devlin, J. P. *J. Phys. Chem.* **1991**, *95*, 90.
(2) Koehler, B. G.; Middlebrook, A. M.; Tolbert, M. A. *J. Geophys. Res. Atmos.* **1992**, *97*, 8065.
(3) Barton, N.; Rowland, B.; Devlin, J. P. *J. Phys. Chem.* **1993**, *97*, 5848.
(4) Radüge, C.; Pflumio, V.; Shen, Y. R. *Chem. Phys. Lett.* **1997**, *274*, 140.
(5) Baldelli, S.; Schnitzer, C.; Shultz, M. J. *J. Phys. Chem. B* **1997**, *101*, 10435.
(6) Donaldson, D. J.; Anderson, D. *Geophys. Res. Lett.* **1999**, *26*, 3625.
(7) Schnitzer, C.; Baldelli, S.; Shultz, M. J. *Chem. Phys. Lett.* **1999**, *313*, 416.
(8) Shultz, M. J.; Schnitzer, C.; Simonelli, D.; Baldelli, S. *Int. Rev. Phys. Chem.* **2000**, *18*, 123.
(9) Yang, H.; Finlayson-Pitts, B. J. *J. Phys. Chem. A* **2001**, *105*, 1890.
(10) Shultz, M. J.; Baldelli, S.; Schnitzer, C.; Simonelli, D. *J. Phys. Chem. B* **2002**, *106*, 5313.
(11) Minogue, N.; Riordan, E.; Sodeau, J. R. *J. Phys. Chem. A* **2003**, *107*, 4436.
(12) Kido Soule, M. C.; Blower, P. G.; Richmond, G. L. *J. Phys. Chem. A* **2007**, *111*, 3349.
(13) Solomon, S. *Rev. Geophysics* **1999**, *37*, 275.
(14) (a) Rivera-Figueroa, A. M.; Summer, A. L.; Finlayson-Pitts, B. *J. Environ. Sci. Technol.* **2003**, *37*, 548. (b) Mochida, M.; Finlayson-Pitts, B. *J. Phys. Chem. A* **2000**, *104*, 9705. (c) Saliba, N. A.; Yang, H.; Finlayson-Pitts, B. *J. Phys. Chem. A* **2001**, *105*, 10339.
(15) (a) Guimbaud, C.; Arens, F.; Gutzwiller, L.; Gäggeler, H. W.; Ammann, M. *Atmos. Chem. Phys. Discuss.* **2002**, *2*, 739. (b) Davies, J. A.; Cox, R. A. *J. Phys. Chem. A* **1998**, *102*, 7631. (c) Beichert, P.; Finlayson-Pitts, B. J. *J. Phys. Chem. A* **1996**, *100*, 15218. (d) Ghosal, S.; Hemminger, J. C. *J. Phys. Chem. B* **2004**, *108*, 14102.
(16) Meilinger, S. K.; Karcher, B.; Peter, Th. *Atmos. Chem. Phys. Discuss.* **2004**, *4*, 4455.
(17) Lawrence, M. G.; Crutzen, P. J. *Tellus* **1998**, *50B*, 263.
(18) Solomon, S.; Borrmann, S.; Garcia, R. R.; Portmann, R.; Thomason, L.; Poole, L. R.; Winker, D.; McCormick, M. P. *J. Geophys. Res.* **1997**, *102*, 21411.
(19) Borrmann, S.; Solomon, S.; Dye, J. E.; Luo, B. *Geophys. Res. Lett.* **1996**, *23*, 2133.
(20) Meier, A.; Hendricks, J. *J. Geophys. Res.* **2002**, 107, (D23), Art. No. 4696.
(21) Abbatt, J. P. D. *Geophys. Res. Lett.* **1997**, *24*, 1479.
(22) It is an important point that nitric acid trihydrate (NAT), which is often implicated in the stratosphere, is not thermodynamically stable under upper troposphere conditions, so that the formation of such a stable hydrate cannot be invoked as an explanation for the ready uptake.
(23) Zondlo, M. A.; Barone, S. B.; Tolbert, M. A. *Geophys. Res. Lett.* **1997**, *24*, 1391.
(24) Zondlo, M. A.; Hudson, P. K.; Prenni, A. P.; Tolbert, M. A. *Annu. Rev. Phys. Chem.* **2000**, *51*, 473.
(25) Hudson, P. K.; Shilling, J. E.; Tolbert, M. A.; Toon, O. B. *J. Phys. Chem. A* **2002**, *106*, 9874.
(26) Bianco, R.; Wang, S.; Hynes, J. T. *J. Phys. Chem. A* **2007**, *111*, 11033.
(27) Bianco, R.; Hynes, J. T. *Theor. Chem. Acc.* **2004**, *111*, 182.

(28) Bianco, R.; Wang, S.; Hynes, J. T. *J. Phys. Chem. B* **2005**, *109*, 21313.
(29) Bianco, R.; Hynes, J. T. *Acc. Chem. Res.* **2006**, *39*, 159.
(30) Bianco, R.; Wang, S.; Hynes, J. T. *Adv. Quantum Chem.* **2008**, *55*, 387.
(31) Shamay, E. S.; Buch, V.; Parrinello, M.; Richmond, G. L. *J. Am. Chem. Soc.* **2007**, *129*, 12910.
(32) Pursell, C. J.; Everest, M. A.; Falgout, M. E.; Sanchez, D. D. *J. Phys. Chem. A* **2002**, *106*, 7764.
(33) Young, T. F., Maranville, L. F.; Smith, H. M. In *The Structure of Electrolyte Solutions*; Hamer, W. J., Ed.; Wiley and Sons: New York, 1959; Chapter 4.
(34) Al-Halabi, A.; Bianco, R.; Hynes, J. T. *J. Phys. Chem. A* **2002**, *106*, 7639.
(35) Marcus, R. A.; Fresco, J. M. *J. Chem. Phys.* **1957**, *27*, 564.
(36) Hudson, P. K.; Schwarz, J.; Baltrusaitis, J.; Gibson, E. R.; Grassian, V. H. *J. Phys. Chem. A* **2007**, *111*, 544.
(37) Peleg, M. *J. Phys. Chem.* **1972**, *76*, 1019.
(38) Irish, D. E.; Brooker, M. H. In *Advances in Infrared and Raman Spectroscopy*; Clark, R. J. H., Hester, R. E., Eds.; Heyden: London, 1976; *Vol. 2*, Chapter 6. For an initial theoretical study of some aspects of $NO_3^-$ symmetry-breaking, see: Ramesh, S. G.; Re, S.; Hynes, J. T. *J. Phys. Chem. A* **2008**, *112*, 3391.
(39) Salvador, P.; Curtis, J. E.; Tobias, D. J.; Jungwirth, P. *Phys. Chem. Chem. Phys.* **2003**, *5*, 3752.
(40) Dang, L. X.; Chang, T. X. M.; Roeselova, M.; Garrett, B. X. C.; Tobias, D. X. J. *J. Chem. Phys.* **2006**, *124*, 066101.
(41) Thomas, J. L.; Roeselova, M.; Dang, L. X.; Tobias, D. J. *J. Phys. Chem. A* **2007**, *111*, 3091.
(42) Morita, A.; Hynes, J. T. *Chem. Phys.* **2000**, *258*, 371. *J. Phys. Chem. B* **2002**, *106*, 673.
(43) Raymond, E. A.; Tarbuck, T. L.; Brown, M. G.; Richmond, G. L. *J. Phys. Chem. B* **2003**, *107*, 546.
(44) Perry, A.; Ahlborn, H.; Space, B. *J. Chem. Phys.* **2003**, *118*, 8411.
(45) Brown, E. C.; Mucha, M.; Jungwirth, P.; Tobias, D. J. *J. Phys. Chem. B* **2005**, *109*, 7934.
(46) Ishiyama, T.; Morita, A. *Chem. Phys. Lett.* **2006**, *431*, 78. *J. Phys. Chem. C* **2007**, *111*, 721; 738.
(47) Stevens, W. J.; Basch, H.; Krauss, M. *J. Chem. Phys.* **1984**, *81*, 6026.
(48) Pietro, W. J.; Francl, M. M.; Hehre, W. J.; DeFrees, D. J.; Pople, J. A.; Binkley, J. S. *J. Am. Chem. Soc.* **1982**, *104*, 5039.
(49) Clark, T.; Chandrasekhar, J.; Spitznagel, G. W.; Schleyer, P. v. R. *J. Comput. Chem.* **1983**, *4*, 294.
(50) (a) Day, P. N.; Jensen, J. H.; Gordon, M. S.; Webb, S. P.; Stevens, W. J.; Krauss, M.; Garmer, D.; Basch, H.; Cohen, D. *J. Chem. Phys.* **1996**, *105*, 1968. (b) Chen, W.; Gordon, M. S. *J. Chem. Phys.* **1996**, *105*, 11081.
(51) Schmidt, M. W.; Baldridge, K. K.; Boatz, J. A.; Elbert, S. T.; Gordon, M. S.; Jensen, J. H.; Koseki, S.; Matsunaga, N.; Nguyen, K. A.; Su, S. J.; Windus, T. L.; Dupuis, M.; Montgomery, J. A. *J. Comput. Chem.* **1993**, *14*, 1347.
(52) Schaftenaar, G.; Noordik, J. H., Molden: a pre- and post-processing program for molecular and electronic structures *J. Comput.-Aided Mol. Design* **2000**, *14*, 123. Molden is available free of charge for academic use at http://www.cmbi.ru.nl/molden/molden.html.
(53) Yamaguchi, Y.; Frisch, M.; Gaw, J.; Schaefer, H. F.; Binkley, J. S. *J. Chem. Phys.* **1986**, *84*, 2262.
(54) Miller, Y.; Gerber, R. B. *Phys. Chem. Chem. Phys.* **2008**, *10*, 1091.
(55) See Figure 1E and Table 1 in: (a) Headrick, J. M.; Diken, E. G.; Walters, R. S.; Hammer, N. I.; Christie, R. A.; Cui, J.; Myshakin, E. M.; Duncan, M. A.; Johnson, M. A.; Jordan, K. D. *Science* **2005**, *308*, 1765.
(56) Ando, K.; Hynes, J. T. *J. Mol. Liq.* **1995**, *64*, 25.
(57) Ando, K.; Hynes, J. T. *J. Phys. Chem.* **1997**, *101*, 10464.
(58) Ando, K.; Hynes, J. T. *J. Phys. Chem. A* **1999**, *103*, 10398.
(59) Gertner, B. J.; Hynes, J. T. *Science* **1996**, *271*, 1563. *Faraday. Discuss.* **1998**, *110*, 301.
(60) Bianco, R.; Hynes, J. T. *J. Phys. Chem. A* **1999**, *103*, 3797.
(61) Rini, M.; Magnes, B.-Z.; Pines, E.; Nibbering, E. T. J. *Science* **2003**, *301*, 349.

JP802563G